4D printed shape memory metamaterial for vibration bandgap switching and active elastic-wave guiding

Received 00th XXXX 20xx,
Accepted 00th XXXX 20xx

DOI: 10.1039/x0xx00000x

Bing Li, [a] Chao Zhang, [b] Fang Peng, [c] Wenzhi Wang, [a] Bryan D. Vogt [d, †] and K.T. Tan [b, *]

Acoustic/elastic metamaterials that rely on engineered microstructures instead of chemical composition enable a rich variety of extraordinary effective properties that are suited for various applications including vibration/noise isolation, high-resolution medical imaging, and energy harvesting and mitigation. However, the static nature of these elastic wave guides limits their potential for active elastic-wave guiding, as microstructure transformation remains a challenge to effectively apply in traditional elastic metamaterials due to the interplay of polarization and structural sensitivity. Here, a tunable, locally resonant structural waveguide is proposed and demonstrated for active vibration bandgap switching and elastic-wave manipulation between 1000-4000 Hz based on 3D printed building blocks of zinc-neutralized poly (ethylene-co-methacrylic acid) ionomer (Surlyn 9910). The ionomer exhibits shape memory behavior to enable rearrangement into new shape patterns through application of thermal stimuli that tunes mechanical performance in both space and time dimensions (4D metamaterial). The thermally induced shape-reorganization is programed to flip a series of frequency bands from passbands to bandgaps and vice versa. The continuously switched bandwidth can exceed 500 Hz. Consequently, altering the bandgap from “on” to “off” produces programmable elastic-wave propagation paths to achieve active wave guiding phenomena. An anisotropic cantilever-in-mass model is demonstrated to predict the self-adaptive dynamic responses of the printed structures with good agreement between the analytical work and experimental results. The tunable metamaterial-based waveguides illustrate the potential of 4D printed shape memory polymers in the designing and manufacturing of intelligent devices for elastic-wave control and vibration isolation.

1. Introduction

Metamaterials through their designed structures produce extraordinary physical properties (like negative/zero permittivity/mass-density/modulus, etc.) that extend beyond those found in natural and composite materials.[1-5] These properties manifest through their engineered subwavelength microstructure that defines the wave propagation rather than intrinsic material characteristics defined by chemistry. The metamaterial design concept has been applied successfully in electromagnetic, thermodynamic, and acoustic fields.[6-13] Recently, significant effort has focused on extending these strategies to elastodynamics for vibration and elastic-wave control.[14-20] Analogous to the optical and acoustic wave control in electromagnetic and acoustic metamaterials, unusual elastic-wave manipulations at subwavelength scale have been realized with elastic metamaterials that provide potential for vibration isolation,[14, 17] negative elastic-wave refraction,[15] cloaking,[21] and unidirectional transmission.[22, 23]

One common drawback for most elastic metamaterials is their passive design, which leads to efficacy only in a designed frequency range. Thus, changes in requirements for the frequency modification of these materials tends to necessitate a full structural re-design.[2, 14, 20, 24, 25] The inherent passive nature of most elastic metamaterials impedes their incorporation in applications where active wave control is necessary. Elastic metamaterials are attractive for active control due to their increased polarization degrees of freedom when compared to electromagnetic and acoustic waves. A downside of this increased freedom is the high sensitivity to localized structural configuration, which adds further handling complexity in the design. To break the restrictions of passive design, one effective approach is to design locally resonant metamaterials and control the microstructures’ resonance frequency in a tunable manner. The corresponding tuning strategy relies on the external stimuli or additional physical coupling induced by smart materials, such as shunted piezoelectric,[26-28] graded functional material,[29] or magneto- and electro-mechanical couplings.[30, 31] However, these strategies add cost and design challenges associated with the need for additional sensors or complicated trigger design and transformation that pose challenges for structural stability and

---

[a] School of Aeronautics, Northwestern Polytechnical University, Xi'an, Shaanxi, 710072, China.
[b] Department of Mechanical Engineering, The University of Akron, Akron, OH 44325-3903, USA.
[c] Department of Polymer Engineering, The University of Akron, Akron, OH 44325-3903, USA.
[d] Department of Chemical Engineering, The Pennsylvania State University, University Park, PA 16802, USA
Corresponding author E-mail address: † bdv5051@psu.edu, * ktan@uakron.edu

Electronic Supplementary Information (ESI) available: Mesh size effects, direct comparison of measured dispersion and calculated transmission, quantification of errors in bandgap from manufacturing inaccuracies and measurement details. [URL will be inserted by publisher] efficient applications. An alternative approach that provides a simpler design is exploiting shape memory effects in alloys or polymers for active design of elastic metamaterials.[32, 33] However, the processing and production of conventional shape memory alloys or polymers are normally limited to structures with simple geometry, which provides less flexible designs for structural manipulation. In consideration of the well-designed microstructures and exquisite configuration, achieving tunable elastic metamaterial using controllably localized shape reconstitution remains a challenge.

Recently, the advancement of 3D printing has enabled the concept of 4D printing, an emerging additive manufacturing strategy for responsive structures.[34-38] 4D printing relies on external stimuli to reshape the configurations of 3D printed structures with time, which provides potential for active and intelligent control. Pioneering work to 4D print mechanical metamaterials has been recently reported.[38-41] Thermally-stimulable shape memory polymers (SMPs) can be printed with temperature-dependent shape tunability,[34, 37, 42-44] which offer a potential route to address challenges pertaining to both complicated structural design and localized shape shifting for active elastic metamaterials. However, most 4D printing reports have focused on the actuation of overall shapes and not the dynamic responses of tunable 4D printed SMP structures. Aiming at controlling the bandgaps by using 4D printing technology, Noroozi et al. proposed two periodically temperature-sensitive architected meta-structures, and numerically investigated their adaptive dynamic characteristics during heating and cooling processes.[45] Zhang et al. presented the self-folding/unfolding performances of controllable lattice and flower-like structures fabricated by 3D printed SMPs with numerical simulations illustrating the potential for active bandgap control.[34] However, this prior research has relied on simulations to predict the potential of bandgap switching in 4D printed shape memory metamaterials, but experimental demonstration of such properties has been elusive. In addition, little work has been reported on tunable elastic waveguides and programmable propagation channels through 4D printed shape memory metamaterials. Simultaneous realization of tunable control, reconfigurability and programmable design over elastic-wave propagation paths is still a great challenge for elastic metamaterials.

In this paper, we demonstrate the design and fabrication of a tunable, locally resonant elastic metamaterial by 4D printed SMPs. The localized self-folding/unfolding performance of the printed shape memory structure is experimentally observed with the impact on bandgap properties clearly shown. To assist with future design, the mechanisms of controllable bandgap properties of the tunable metamaterial were theoretically analyzed and shown to agree with the experimentally determined dynamic bandgaps. The self-adaptive bandgap switching is experimentally measured, and further applied to the design of tunable, programmable elastic-wave propagation channels.

2. Materials and design

2.1. Structural design and fabrication

A schematic of the proposed shape memory elastic metamaterial is illustrated in Fig. 1(a). In consideration of the effective local-resonance performance of cantilevered beams,[8, 46, 47] the unit cell of the periodic structure is designed as a snowflake shape to provide a simple, yet effective cell design for mechanical metamaterials. The honeycomb periodic array is selected due to its known utility for elastic metamaterials. For the snowflake-like structure, it is expected that the branched "snow petals" inside unit cells can be intentionally deformed to a folded configuration after undergoing a heating and cooling process. Afterward, based on the shape memory mechanism, the reshaped pillars can self-adaptively switch back from a folded status to the initially unfolded configuration under thermal excitation. Consequently, the dispersion spectra and bandgap characteristics of the tunable elastic metamaterial can be actively controlled. The shape reconstructions are limited to the internal and localized "snow petals", which can be considered as auxiliary structures to the main frame.

To fabricate the designed structure, a Cartesio W09 3D printer is used and the 3D printing process is schematically presented in Fig. 1(b). The extrusion-based printing technology, fused deposition modelling (FDM), is applied here, and the base material of the filament is an ionomeric thermoplastic SMP, zinc-neutralized polyethylene-co-methacrylic acid (PEMA, DuPont, Surlyn 9910) ionomer, which is provided by Dow Corning Corporation. We have previously demonstrated that this commercially available PEMA can be readily adopted to FDM printing.[37] The filaments of Surlyn were extruded using a HAAKE single-screw extruder (Model Rheomex 252p, see Fig. 1(c)). The extruder was equipped with a gear pump and a simple circular die with a diameter of 2.2 mm. Prior to extrusion, Surlyn pellets (as obtained from DuPont) were dried in a vacuum oven for 12 h at 60 °C to remove absorbed moisture, which can lead to degradation during melt processing. The temperature profile used for filament extrusion is shown in Table 1. The extruded filaments were quenched in a room-temperature water bath and drawn onto a take-up spool by two take up rollers. The diameter of the filaments was drawn down to 1.70 ± 0.03 mm. During 3D printing fabrication, a Kapton tape was used to cover the platform-bed to improve the adhesion during the print, while easily releasing the printed specimen from the bed when completed. A constant bed temperature of 40 °C was used, and the extrusion temperature of the nozzle was set to 260 °C. The printing velocity was set to 10 mm/s with a layer height of 0.2 mm. The G-code of printing commands was programmed by commercial software Slic3r.

For this type of Surlyn PEMA, the Fourier transform infrared spectrum is illustrated in Fig. 1(d). The strong and intense band at 1465 cm^{-1} corresponds to the –CH2– bending and a weak band at 1374 cm^{-1} indicates that –CH2– wagging presents zinc ionomer. The zinc ionomer also exhibits a broad absorption peak around 1540 cm^{-1} in the asymmetric carboxylate stretching region. This broad band is associated with the coupled asymmetric carboxylate vibration of zinc carboxylate ions present in the neat ionomers. The C=O stretching vibration is typical of the ester/acid carbonyl groups at 1698 cm^{-1} and region below 1600 cm^{-1} presents some difference in the profile pattern of the absorptions. The carbonyl absorption region presents the ester/acid absorptions at 1720 cm^{-1} and the asymmetric carboxylate stretching band near 1582 cm^{-1}.

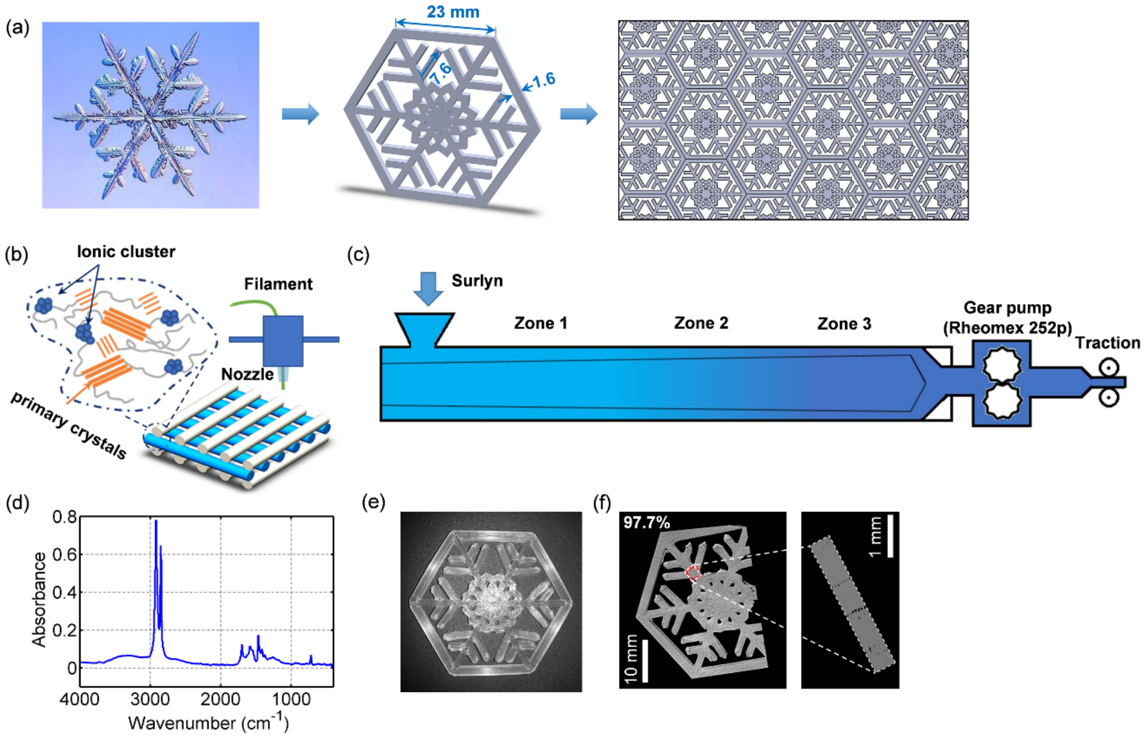

Fig. 1 (a) Schematic of the proposed tunable elastic metamaterial consisting of snowflake like unit cells, (b) FDM-based 3D printing and the molecular structure of the PEMA filament. (c) Schematic of the extrusion process Surlyn filaments. (d) Fourier transform infrared spectrum of Surlyn. (e) A printed shape memory unit cell and (f) its 3D X-ray micro-computed tomography with 10 mm and 1 mm scale bars.

By using the above material and fabrication technique, a printed snowflake-like unit cell is shown in Fig. 1(e). To evaluate the infill density of the specimen after 3D printing, X-ray micro-computed tomography (General Electric Phoenix Nanotom-MTM 180 X-ray tomography system) was used to characterize the internal structure. The tomographic radiographs were acquired with an accelerating voltage of 125 kV and a beam current of 180 µA. Each single image was collected from 1800 rotation views over 360° of rotation (0.225 degree per rotation step). Then the 3D tomographic images, as presented in Fig. 1(f), were reconstructed by using Phoenix software and VG Studio Max software. It is shown in Fig. 1(f) that the pore gap is small with the infill density calculated from Fig. 1(f) to be approximately 97.7%, thereby demonstrating that sufficient printing quality of the shape memory material can be obtained.

Table 1 Temperature Profile for Filament Extrusion.

Zone 1 (°C)	Zone 2 (°C)	Zone 3 (°C)	Gear pump (°C)	Die (°C)
220	230	240	240	200

2.2. Shape memory performance

To verify the shape memory behaviour, the self-adaptive unfolding performance of one snowflake-like unit cell was tested. The initial or permanent shape of the printed unit cell is denoted as S0 (see Fig. 2). Then the bottom surface of the printed unit cell was heated by a heating platform with a temperature of 65 °C ~70 °C and the inside long straight "petals" were stretched by a tweezer to deform into a temporary folded status (S1). This folded shape was fixed by quenching in an ice water bath at around 0 °C. For shape recovery, the folded unit cell was laid flat again on the heating platform. Under a continuous thermal stimulus of 65 °C~70 °C, the folded "petals" recovered to their permanent state within 5 min (from S1 to S6, additional details are included in the supplementary video). Comparing the recovered pattern with the original permanent topology (S0), the shape memory effect is macroscopically verified, and the self-adaptively localized shape modification is realized.

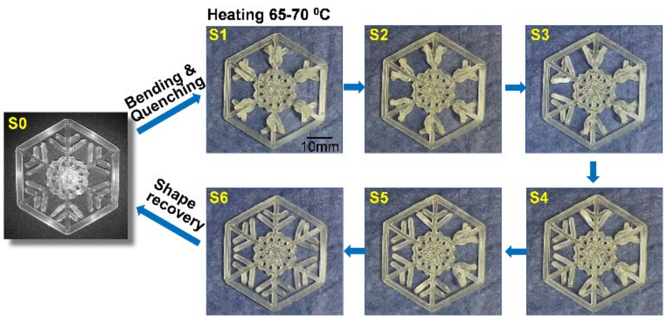

Fig. 2 Shape memory cycle for the printed snowflake-like unit cell from permanent shape (S0) to the temporary (S1-S5) and to the recovered shapes (S6).

3. Results and discussion

3.1. Dispersion spectrums

To investigate the effect of shape recovery on dispersion spectrums of the periodic metamaterial structure, we first calculated the band structure diagrams numerically based on the Bloch-Floquet theory. A commercial software, COMSOL Multiphysics, is utilized to build the models of snowflake-like unit cells with three configurations to approximately mimic the recovery process from folded to unfolded status (see Fig. 3). The Floquet periodicity boundary conditions are applied on pairs of parallel faces of each unit cell, resulting in an infinite periodic plate-waveguide, where

$$u_{dst} = u_{src} e^{-i\kappa_F (r_{dst} - r_{src})} \tag{1}$$

κ_F is the Floquet wavenumber, u is the displacement and r is the spatial coordinates of the periodic boundaries. Subscripts src and dst indicate a variable defined at the source and the destination, respectively.

The periodic symmetry of a honeycomb array follows the primitive lattice vectors of a hexagonal lattice. The first Brillouin zone (FBZ) is depicted as the hexagon in Fig. 3(a), which is obtained by the adjacent points of the reciprocal lattice. The irreducible Brillouin zone (IBZ, see the region ΓMK in Fig. 3(a)) represents the smallest part of the FBZ, which describes all the high symmetry points for wave propagation analysis. The corresponding wave vectors of high symmetry points are $\Gamma(k_x{=}0,\ k_y{=}0)$, $\mathrm{M}(k_x{=}0,\ k_y{=}\frac{2\pi}{\sqrt{3}l_a})$, $\mathrm{k}(k_x{=}\frac{2\pi}{3l_a},\ k_y{=}\frac{2\pi}{\sqrt{3}l_a})$, where l_a is the distance between two adjacent unit cells.

The dispersion relation spectrums are numerically calculated by the finite element models built by COMSOL Multiphysics. The *Solid Mechanics* module is selected, and an *Eigenvalue* problem is studied. The periodic connection conditions of Floquet periodicity are applied to the edges of unit cell. A parametric sweep of wave vectors, k_x and k_y, along the IBZ edge (Γ-M-K-Γ) are conducted to determine the eigenfrequencies, then the dispersion spectrums can be drawn by the global evaluation. The study of mesh independency is discussed in the Electronic Supplementary Information (ESI).

For an infinite structure with a honeycomb array of the stretched unit cell (Unit cell I), the numerical dispersion relation spectrum is illustrated in Fig. 3(a). Two other unit cells with curved or without long inside "petals" (Unit cells II and III, see Fig. 3(b)), which approximately simulate two other shapes obtained during the shape recovery process (see Fig. 2), are examined for comparison. Three typical frequency ranges are selected to compare the band structures of the proposed metamaterial under various recovery configurations. As depicted in Figs. 3(b)-3(d), there are a series of complete or directional bandgaps (regions shaded by yellow) around 1140 Hz, 1790 Hz, 2150 Hz and 2700-2800 Hz for Unit cell I, which can block the wave propagation and significantly attenuate the wave transmission at these frequencies. However, for Unit cells II and III, the bandgaps shift and even vanishing in some cases due to the structural reconfiguration. These changes can transform bandgap (or passband) regions for the permanent structure (Unit cell I) to passbands (or bandgaps) for the temporary structures that can be tuned through the shape memory recovery (Unit cells II and III). The adaptive function for open and closing of bandgaps through thermally activated shape memory recovery provides potential to realize the active "on" or "off" control of elastic-wave transmission.

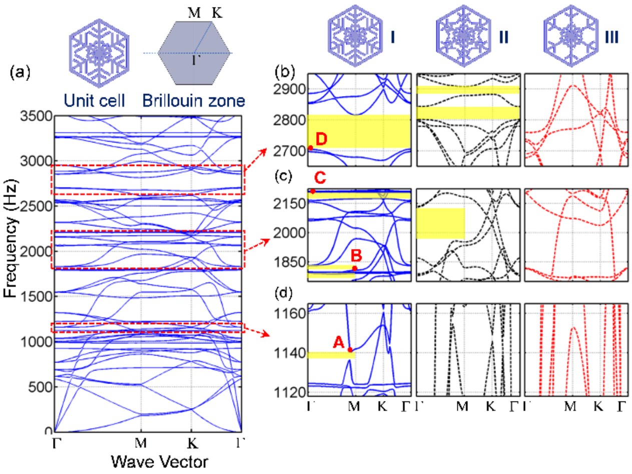

Fig. 3 (a) Brillouin zone and dispersion spectrum of an infinite metamaterial consisting of snowflake-like unit cells (Unit cell I). (b) Comparisons of bandgap characteristics at different stages in shape recovery (Unit cells I, II, III) within the frequency ranges of 2650-2950 Hz, (c) 1750-2225 Hz and (d) 1118-1165 Hz.

To more deeply understand the bandgap mechanisms, the resonant modes at four representative frequencies close to the identified bandgaps (see frequencies A-D in Fig. 3) are examined to visually illustrate the coupling effect between the "snowflake" frame and the branched "petals". As shown in Fig. 4, for the narrow directional bandgap around the frequency A (1140.2 Hz), the resonance mode is induced by both frame and inside pillars, but mainly induced by the pillars. Around the other three bandgaps (frequencies B-D), the snowflake-like unit cell presents distinct locally resonant profiles. The displacement field distributions of these eigenstates are localized within the branched "petals" alone, whereas the host frame confines almost no vibration. Therefore, all bandgaps in this structural motif can be modulated simply by controlling the petals' configurations. Based on the mode shapes captured at the bandgap boundaries, we can specify that the bandgaps below 3000 Hz are induced by the petals' local resonances, while Bragg type bandgaps occur at frequencies greater than 3000 Hz (see Fig. 3(a)).

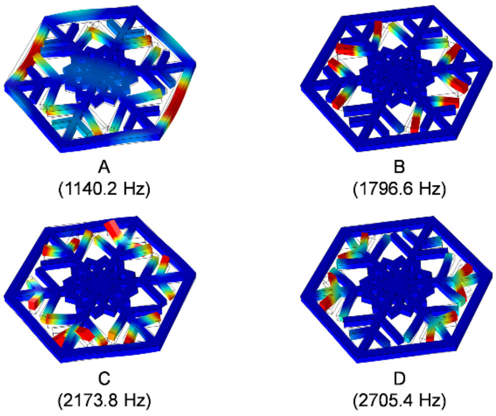
A
(1140.2 Hz)
B
(1796.6 Hz)
C
(2173.8 Hz)
D
(2705.4 Hz)

Fig. 4 Resonant modes of Unit cell I at four representative frequencies of A-D near proximity of bandgaps.

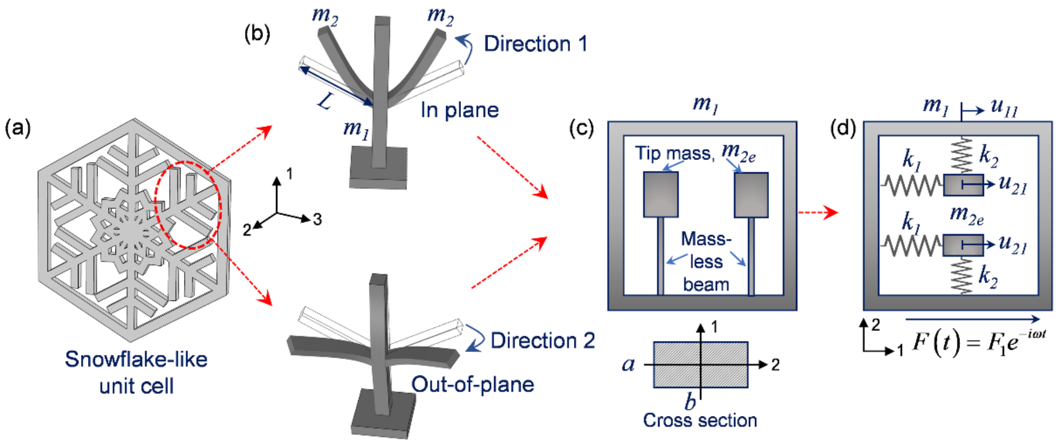

Fig. 5 Primary flexural vibration modes along two orthogonal orientations: (a) direction 1 and (b) direction 2. (c) Equivalent cantilever-in-mass model and (d) 2D anisotropic mass-spring lattice system for the snowflake-like unit cell.

3.2. Theoretical analysis on locally resonant bandgaps

To predict and tailor the bandgap frequencies, a cantilever-in-mass model is developed to theoretically analyse the effect of branched "petals" on the locally resonant bandgaps. As shown in Fig. 5, the frame of the snowflake-like unit cell can be represented as a holding base, and the inside "petals" can be treated as branched beams. For simplicity, only one group of "petals" with a length of L are analyzed as geometrically these are equivalent. Based on the locally resonant mode shapes exhibited in Fig. 4, two primary flexural vibration modes along two orthogonal orientations, directions 1 and 2 (see Figs. 5(a) and 5(b)), are theoretically examined. The holding base can be described by an outer mass of m_1; the branched beam can be represented by a tip mass of m_{2e} and a massless cantilever beam with the same length of L (see Fig. 5(c)). Furthermore, we can transform this cantilever-in-mass model into an equivalent two dimensional (2D) anisotropic mass-spring lattice system, as illustrated in Fig. 5(d). The flexural vibration modes along two orthogonal directions can be enacted by the harmonic motions of two orthogonal springs.

On basis of Euler-Bernoulli beam theory and Hooke's law, the equivalent spring stiffness k_1 and k_2 in the lattice system[8] can be written as $k_i = 3EI_{zi}/L^3$, $i = 1,2$, where E is the Young's modulus and I_{zi} is the moment of inertia with respect to the bending axis of the two flexural modes. It can be assessed that $I_{z1} = ab^3/12$ for direction 1 and $I_{z2} = a^3b/12$ for direction 2, where a and b are the width and thickness of the beam cross section, respectively. For the 2D mass-spring model under a longitudinal harmonic force excitation along direction 1 ($F(t) = F_1e^{-i\omega t}$, see Fig. 5(d)), it is assumed that there is no coupling between the two flexural modes along the orthogonal directions.

For harmonic wave propagation ($u_{j1} = U_{j1}e^{-i\omega t}, j = 1,2$), the equations of motion can be derived as

$$\begin{bmatrix} 2k_1 - m_1\omega^2 & 2k_1 \\ -k_1 & k_1 - m_{2e}\omega^2 \end{bmatrix}\begin{bmatrix} U_{11} \\ U_{21} \end{bmatrix} = \begin{bmatrix} F_1 \\ 0 \end{bmatrix} \quad (2)$$

By substituting the locally resonant frequency of m_{2e} along direction 1, $\omega_{21} = \sqrt{k_1/m_{2e}}$, into Eq. (2), and describing the mass-spring unit cell by a single effective mass of m_{eff1},[8, 23] we can obtain $m_{eff1} = m_1 + 2\omega_{21}^2 m_{2e}/(\omega_{21}^2 - \omega^2)$. Similarly, we can also obtain the effective mass for the flexural mode along direction 2, m_{eff2}. Then the internal coupling effects between branched "petals" and the host frame can be mathematically evaluated by an effective anisotropic mass as

$$\begin{cases} m_{eff,j} = m_1 + \dfrac{2\omega_{2j}^2 m_{2e}}{\omega_{2j}^2 - \omega^2} \\ \omega_{2j} = \sqrt{\dfrac{3EI_{zj}}{L^3 m_{2e}}} \end{cases}, j = 1,2 \quad (3)$$

The tip mass m_{2e} at the free end can be estimated as $m_{2e} = 0.236m_2$ based on the continuum beam theory and kinetic energy analysis.[8] Then the effective anisotropic mass and the two locally resonant frequencies can be further written as

$$\begin{cases} m_{eff,j} = m_1 + \dfrac{0.47\rho abL\omega_{2j}^2}{\omega_{2j}^2 - \omega^2}, j = 1,2 \\ \omega_{21} = \dfrac{b}{L^2}\sqrt{\dfrac{1.06E}{\rho}}, \quad \omega_{22} = \dfrac{a}{L^2}\sqrt{\dfrac{1.06E}{\rho}} \end{cases} \quad (4)$$

Based on this theoretical basis, the effect of branched petal's length on the locally resonance frequencies were calculated and plotted in Fig. 6. Although the deformation of snowflake unit cell during the shape memory process is more complicated than solely changing the petal's length change, this model can qualitatively describe the influence of shape recovery on the locally resonant behaviour in a simplified way. Fig. 6 indicates that the locally resonant frequencies for both directions decrease with the increase of petal's length, while the locally resonant frequency along direction 1 is always lower than that along direction 2. For the unfolded status, the axis length of the long petals is around 7.6 mm (see Fig. 1(a)). According to Eq. (4), the theoretical locally resonant frequencies along the two directions are 1862.2 Hz and 2327.8 Hz, respectively, which have very good agreement with the upper limits of the numerical bandgaps (1835 Hz and 2213 Hz) around mode shapes B and C (see Fig. 3). The relative errors are 1.5% and 5.19%, respectively. It is theoretically evident that the local resonances of inside "petals", leading to bandgaps, can be actively manipulated by the self-adaptive shape memory process.

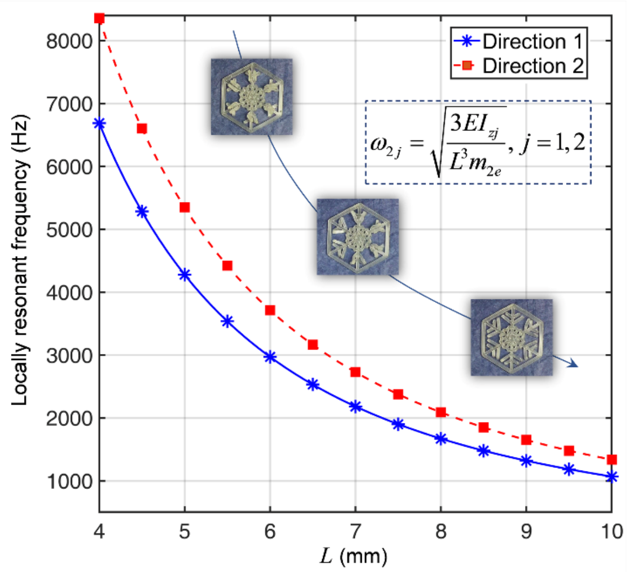

Fig. 6 Effect of branched petal's length on the locally resonance frequencies along directions 1 and 2 determined from a simplified cantilever-in-mass model.

3.3. Tunable bandgaps and programmable waveguides

Dynamic experimental testing is performed to experimentally investigate the bandgap switching and shifting of the tunable metamaterial based on the 3D printed PEMA structures. As illustrated in Fig. 7, a PEMA specimen consisting of 2 × 6 snowflake-like unit cells was fabricated by 3D printing and assembly. The dimension of the whole structure is 290 mm×80 mm×2 mm.

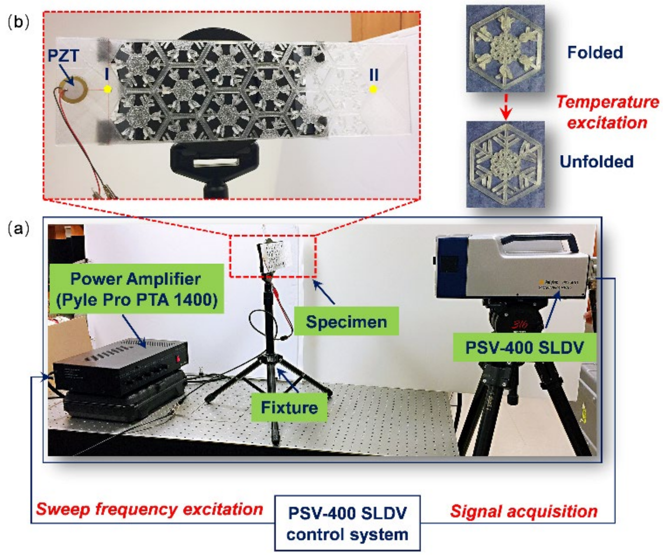

Fig. 7 (a) Experimental setup for the FRF measurement of the 4D printed tunable metamaterial under two shape recovery status. (b) Excitation and output points for experimental testing.

As shown in Fig. 7(b), a PZT wafer (diameter=20 mm) is bonded on the surface of the metamaterial plate to generate guided waves. A sweep sinusoidal tone burst with the frequency range of 800-4000 Hz is generated with a scanning laser Doppler vibrometer (Polytec, PSV-400), amplified by a power amplifier (Pyle Pro PTA1400) and then input to the PZT actuator. Two points, I and II, located before and after the metamaterial part are selected to calculate the frequency response function (FRF). The scanning laser vibrometer is utilized to collect the out-of-plane velocity at the two testing points. The experimental transmission ratios at different frequencies are obtained by the ratio of the output signal captured at Point II to the input signal captured at Point I. The reported transmission ratios are a result of 100 individual measurements to improve the signal-to-noise ratio. The sampling frequency is set as 10.24 kHz and the sampling time is 1.6 s.

Dynamic responses of the proposed active metamaterial structure under two shapes are experimentally measured. For the first status, the "petals" of snowflake-like unit cells are folded, while for the second scenario they recover from folded to unfolded after a heating excitation (around 65 °C~70 °C, 5 minutes). The maximum transmission ratio is used to normalize the transmission ratio-frequency profiles, and the normalized results for the two structural states are depicted and compared in Fig. 8(a). Several bandgaps are experimentally measured in both states. For the unfolded state, the two bandgaps around 1900 Hz and 2250 Hz agree well with the theoretical predictions of 1862.2 Hz and 2327.8 Hz from mode shapes B and C. More interestingly, an obvious shift in the bandgap ranges is observed between the folded and unfolded states; some frequency bands switch from passbands/bandgaps to the opposite bandgaps/passbands through the thermally activated shape recovery (shape memory effect). Specifically, the passband around 2250 Hz switches to a broader bandgap (regions shaded by green), while a bandgap around 1800 Hz switches back to a passband when the folded petals unfold adaptively. The continuously switched bandwidth can exceed 500 Hz for this simple transformation based on shape memory. These results experimentally demonstrate that the bandgaps of the proposed metamaterial can be actively controlled from "on (off)" to "off (on)" by the adaptive shape memory effect.

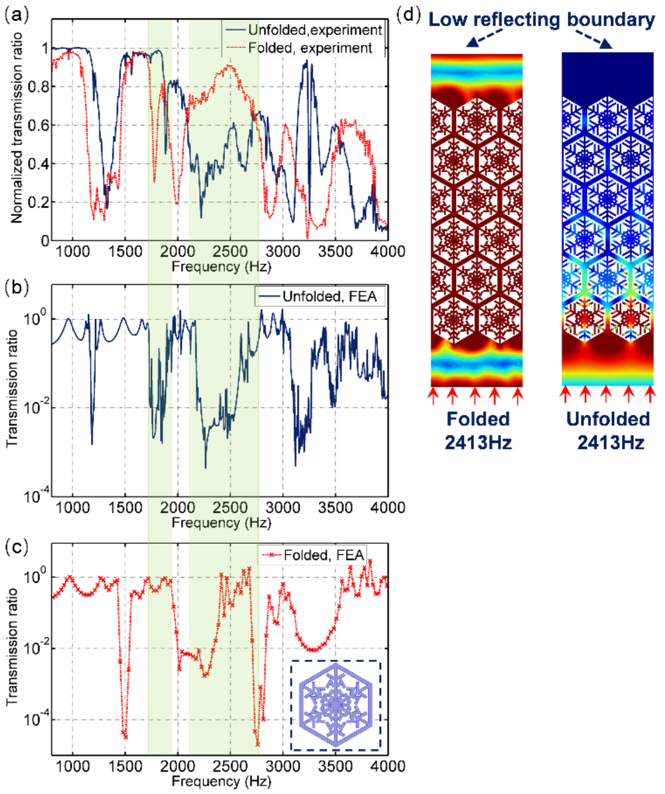

Fig. 8 (a) Experimental transmission ratio-frequency profiles under the unfolded and folded status. (b) Numerical transmission ratio-frequency profiles under the unfolded and (c) folded status. (d) Switch between elastic-wave propagation and attenuation in the tunable metamaterial at the same frequency.

Numerical transmission spectrums are further performed to more quantitatively describe the tunable bandgaps. The transmission responses are evaluated in a sweep frequency domain. A time harmonic displacement is applied to the left end of the plate-like structure, while a low-reflecting boundary is applied to the right end. For the structure with unfolded “petals”, the simulated transmission ratio-frequency profile is exhibited in Fig. 8(b). In general, the simulated transmission spectrum agrees qualitatively with the experimental FRF. The calculated transmission spectrum is also in good agreement with the experimentally measured dispersion curve (see ESI). The mismatch for a couple of bandgaps could be a result of the combination of imperfections in manufacturing and the measurement accuracy (see ESI). The exact simulation of the folded state is more challenging as the structure is non-planar experimentally, the model of folded unit cell is simplified as illustrated in the inset of Fig. 8(c). Comparison of the numerical transmission spectra under the two states leads to the same general conclusions as from the experimental measurements. As shown in the shaded regions in Figs. 8(b) and (c), the switch between bandgap and passband is numerically captured and verified for the folded and unfolded states.

The displacement distribution contours captured at a representative frequency of 2413 Hz under the two states are presented and compared in Fig. 8(d). This frequency belongs to a passband in the folded state, but switches to a bandgap frequency in the unfolded state. Fig. 8(d) shows that significant wave transmission at the output side occurs when the “petals” are folded. However, when the “petals” unfold to the straight state, wave propagation is blocked at the input side and an extremely weak transmitted wave is observed. The bandgap shifting and switching effect from “on” to “off” is thus further illustrated through these analyses. It can be concluded from both experimental and numerical verifications that the bandgap characteristics and transmission properties of the 4D printed shape memory metamaterial can be actively manipulated by the self-tunable shape recovery effect.

Based on the tunable transmission properties, we can further design programmable channels and actively control the propagation paths of elastic-waves. As shown in Fig. 9(a), if the unfolded and folded unit cells are respectively defined as digital elements “0” and “1”, we can readily build a “Z” shape channel. We use “On” (010) and “Off” (000) to indicate the folded and unfolded unit cells in the “Z” channel, which can be actively switched by the shape memory effect. The excitation region is indicated by a yellow star. As shown in Fig. 9(b), in the “On” state, the generated elastic-waves can propagate exactly along the “Z” shape path through the digital elements, which can turn around two opposite corners with high transmission. In contrast, by switching to “Off”, the propagation path is correspondingly eliminated (see Fig. 9(c)). In this case, the elastic-waves cannot propagate due to the bandgap effect.

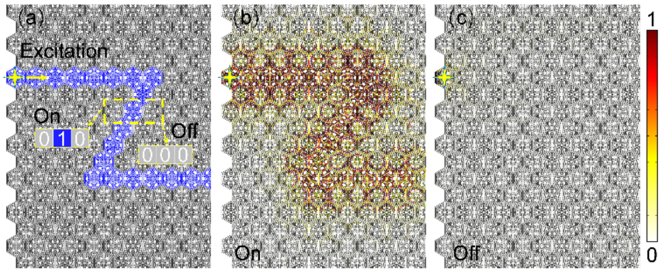

Fig. 9 (a) Programmable “Z” shape elastic-wave propagation path composed of two digital elements of “0” and “1”. Distributions of normalized displacement field in the programmable waveguide with the “Z” shape channel (b) at the “On” state and (c) “Off” state.

Besides providing a pathway for passing the elastic wave through the structure, the programmable elements could also guide the elastic-wave to make a U-turn (see Fig. 10). Fig. 10(a) illustrates the “U” shape channel with two programmable states.

As exhibited in Fig. 10(b), for the “On” state (010), the incident elastic-waves can transmit along the designed path, make a smooth U-turn as expected, then propagate back to the excitation side with high transmission. When it switches to “Off” status (000), the input elastic-waves are blocked at the input side (see Fig. 10(c)) and cannot transmit through the waveguide. A reference region circled by yellow dotted line in Fig. 10(b) is selected to quantitatively evaluate the tunable propagation properties. The out-of-plane displacements captured in the selected regions for “On” and “Off” states are compared in Fig. 10(d). It is evident that in the “On” state, the response amplitude around the designed channel zone is much higher than that of the other regions. In the “Off” state, the amplitudes in the whole region decrease dramatically, which would result in a tremendous loss in the waveguiding of the channel zone in comparison to when the material is in the “On” state.

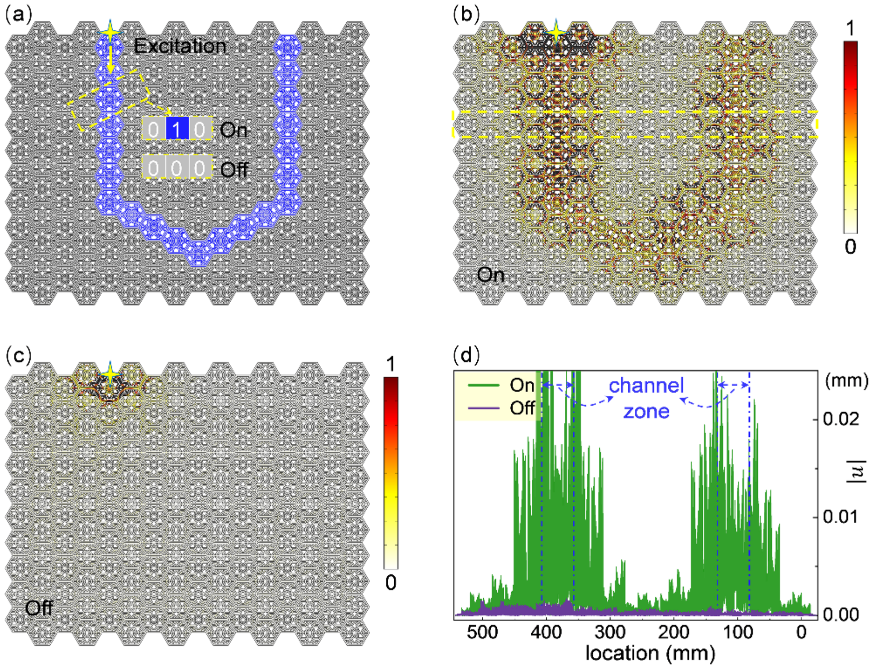

Fig. 10 (a) Programmable "U" shape propagation path composed of two digital elements of "0" and "1". Distributions of normalized displacement field in the programmable waveguide with the "U" shape channel (b) at the "On" state and (c) "Off" state. (d) Comparison of the displacement distribution profiles at "On" and "Off" states.

Moreover, we can use the programmable elements to build a closed-loop channel, as shown in Fig. 11(a). To verify its robustness, the closed-loop channel is designed as a heart shape. The excitation region is indicated by the star. As observed in Fig. 11(b), at the "On" status, the input energy is guided and locked in the heart-shape channel, and can hardly transmit into the other region. This demonstrates an efficient vibration isolation waveguide based on the programmable design. Based on these results, we can deduce that the proposed shape memory metamaterial can realize tunable, programmable elastic-wave propagation channels with arbitrary shapes. Switching of the elastic waveguides can be actively controlled by the shape memory effect.

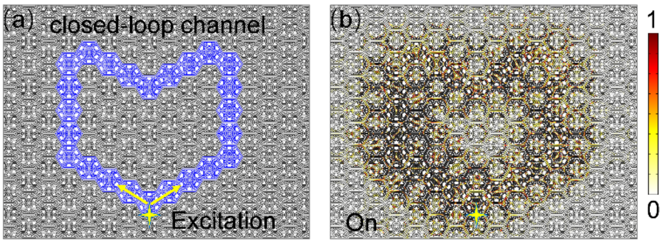

Fig. 11 (a) Programmable closed-loop propagation channel with a heart shape. (b) Distribution of energy density field in the programmable waveguide with the closed-loop channel ("On" state).

4. Conclusions

In summary, we have proposed and demonstrated a tunable shape memory elastic metamaterial for self-adaptive bandgap switching and programmable elastic-wave propagation paths. Based on the emerging concept of 4D printing, the designed structural waveguide can be effectively fabricated by using a thermoplastic, semicrystalline ionomer (PEMA, DuPont, Surlyn 9910) in FDM printing without any additional chemistry requirements. The robust shape memory behaviour and spontaneously localized structural recovery have been experimentally realized. The desirably tunable bandgap control in the proposed metamaterial has been numerically and experimentally verified. The mechanisms of tunable bandgap properties have been systematically analyzed. An anisotropic cantilever-in-mass model has been developed to predict the locally resonant responses of the tunable metamaterial; good agreements between analytical, numerical and experimental bandgaps have been obtained. By virtue of the self-adaptive unfolding of the 4D printed shape memory meta-structure, programmable propagation paths and active elastic-wave guiding have been realized by switching the bandgap from "on" to "off". This study offers new opportunities to designing and manufacturing intelligent structural waveguide for active vibration and elastic-wave manipulation, which extends the pathway for the application of 3D printed thermoplastic SMPs.

Conflicts of interest

There are no conflicts to declare.

Acknowledgements

B. Li acknowledges financial support from the National Natural Science Foundation of China under Grant No. 11902262. K.T. Tan acknowledges financial support for this research from the Faculty Research Committee (FRC) of The University of Akron (FRG Account Number 1864). F.P. and B.D.V. acknowledge partial support of this work from the National Science Foundation under Grant No. Grant CMMI-1825276 and CMMI-2011289.

Notes and references

1 S. A. Cummer, J. Christensen and A. Alù, *Nat. Rev. Mater.*, 2016, **1**, 16001.
2 G. Ma and P. Sheng, *Sci. Adv.*, 2016, **2**, e1501595.
3 K. Bertoldi, V. Vitelli, J. Christensen and M. Hecke, *Nat. Rev. Mater.*, 2017, **2**, 17066.
4 Z. Liu, X. Zhang, Y. Mao, Y. Y. Zhu, Z. Yang, C. T. Chan and P. Sheng, *Science*, 2000, **289**, 1734–1736.
5 M. H. Lu, L. Feng and Y. F. Chen, *Mater. Today*, 2009, **12**, 34-42.
6 R. A. Shelby, D. R. Smith and S. Schultz, *Science*, 2001, **292**, 77-79.
7 T. C. Han, P. Yang, Y. Li, D. Lei, B. W. Li, K. Hippalgaonkar and C. W. Qiu, *Adv. Mater.*, 2018, **30**, 1804019.
8 B. Li, K. T. Tan and J. Christensen, *Phys. Rev. B,* 2017, **95**, 144305.
9 T. J. Cui, S. Liu and L. Zhang, *J. Mater. Chem. C*, 2017, **5**, 3644-3668.
10 L. Fok, M. Ambati and X. Zhang, *MRS Bull.*, 2008, **33**, 931-934.
11 F. Ma, J. Chen and J. H. Wu, *J. Mater. Chem. C*, 2019, **7**, 5131–5138.
12 Y. H. Liao, X. M. Zhou, Y. Y. Chen and G. L. Huang, *Smart Mater. Struct.*, 2018, **28**, 025005.
13 Y. F. Wang, Y. Z. Wang, B. Wu, W. Chen and Y. S. Wang, *Appl. Mech. Rev.*, 2020, **72**, 040801.
14 Z. Wang, Q. Zhang, K. Zhang and G. Hu, *Adv. Mater.*, 2016, **28**, 9857-9861.
15 R. Zhu, X. N. Liu, G. K. Hu, C. T. Sun and G. L. Huang, *Nat. Commun.*, 2014, **5**, 5510.
16 B. Li, Z. Li, J. Christensen and K. T. Tan, *Appl. Phys. Lett.*, 2019, **114**, 081906.
17 Z. C. He, X. Xiao and E. Li, *Compos. Part B: Eng.*, 2017, **131**, 237-252.
18 Y. Liu, Z. Liang, J. Zhu, L. Xia, O. Mondain-Monval, T. Brunet, A. Alù and J. Li, *Phys. Rev. X*, 2019, 9, 011040.
19 Q. Q. Li, Z. C. He, E. Li, P. Liu, X. Y. Lin and Y. Wu, *Smart Mater. Struct.*, 2020, **29**, 045042.
20 H. Liu, Q. Zhang, K. Zhang, G. Hu and H. Duan, *Adv. Sci.*, 2019, **6**, 1900401.
21 F. Liu and Z. Liu, *Phys. Rev. Lett.*, 2015, **115**, 175502.
22 S. H. Mousavi, A. B. Khanikaev and Z. Wang, *Nat. Commun.*, 2015, **6**, 8682.
23 S. Alamri, B. Li, G. Mchugh, N. Garafolo and K.T. Tan, *J. Sound Vib.*, 2019, **451**, 120-137.
24 P. Celli, S. Gonella, V. Tajeddini, A. Muliana, S. Ahmed and Z. Ounaies, *Smart Mater. Struct.*, 2017, **26**, 035001.
25 P. Wang, F. Casadei, S.H. Kang and K. Bertoldi, *Phys. Rev. B*, 2015, **91**, 020103.
26 A. Bergamini, T. Delpero, L. D. Simoni, L. D. Lillo, M. Ruzzene and P. Ermanni, *Adv. Mater.*, 2014, **26**, 1343-1347.
27 F. Casadei, T. Delpero, A. Bergamini, P. Ermanni and M. Ruzzene, *J. Appl. Phys.*, 2012, **112**, 064902.
28 R. Zhu, Y. Y. Chen, M. V. Barnhart, G. K. Hu, C. T. Sun and G. L. Huang, *Appl. Phys. Lett.*, 2016, **108**, 011905.
29 H. Jafari, S. Sepehri, M.R. Yazdi, M.M. Mashhadi and M.M. Fakhrabadi, *Acta Mech.*, 2020, **3**, 1-5.
30 Y. F. Wang, B. Yousefzadeh, H. Chen, H. Nassar, G. L. Huang and C. Daraio, *Phys. Rev. Lett.*, 2018, **121**, 194301.
31 A. Bayat and F. Gordaninejad, *Smart Mater. Struct.*, 2015, **24**, 065027.
32 K. C. Chuang, X. F. Lv and D. F. Wang, *Appl. Phys. Lett.*, 2019, **114**, 051903.
33 V. C. Sousa, D. Tan, C. D. Marqui and A. Erturk, *Appl. Phys. Lett.*, 2018, **113**, 143502.
34 Q. Zhang, K. Zhang and G. K. Hu, *Sci. Rep.*, 2016, **6**, 22431.
35 X. Kuang, D. J. Roach, J. T. Wu, C. M. Hamel, Z. Ding, T. J. Wang, M. L. Dunn and H. J. Qi, *Adv. Funct. Mater.*, 2019, **29**, 1805290.
36 A. Mitchell, U. Lafont, M. Holynska and C. Semprimoschnig, *Addit. Manuf.*, 2018, **24**, 606-626.
37 Z. Y. Zhao, F. Peng, K. A. Cavicchi, M. Cakmak, R. A. Weiss and B. D. Vogt, *ACS Appl. Mater. Interfaces*, 2017, **9**, 27239-27249.
38 X. Wan, L. Luo, Y. Liu and J. Leng, *Adv. Sci.*, 2020, **7**, 2001000.
39 M. Bodaghi, A. Serjouei, A. Zolfagharian, M. Fotouhi, H. Rahman and D. Durand, *Int. J. Mech. Sci.*, 2020, **173**, 105451.
40 M. Bodaghi and W. H. Liao, *Smart Mater. Struct.*, 2019, **28**, 045019.
41 C. Yang, M. Boorugu, A. Dopp, J. Ren, R. Martin, D. Han, W. Choi and H. Lee, *Mater. Horiz.*, 2019, **6**, 1244-1250.
42 Y. Yang, Y. H. Chen, Y. Wei and Y. T. Li, *Int. J. Adv. Manuf. Tech.* 2016, **84**, 2079-2095.
43 Y. Q. Mao, Z. Ding, C. Yuan, S. G. Ai, M. Isakov, J. T. Wu, T. J. Wang, M. L. Dunn and H. J. Qi, *Sci. Rep.*, 2016, **6**, 24761.
44 Z. Ding, C. Yuan, X. R. Peng, T. J. Wang, H. J. Qi and M. L. Dunn, *Sci. Adv.*, 2017, **3**, e1602890.
45 R. Noroozi, M. Bodaghi, H. Jafari, A. Zolfagharian and M. Fotouhi, *Polymers*, 2020, **12**, 519.
46 A. Qureshi, B. Li and K.T. Tan, *Sci. Rep.*, 2016, **6**, 28314.
47 S. Sepehri, H. Jafari, M.M. Mashhadi, M.R.H. Yazdi and M.M.S. Fakhrabadi, *Int. J. Solids and Struct.*, 2020, **204**, 81-95.